# Gas-phase spectroscopy of photostable PAH ions from the mid- to far-infrared

Sandra D. Wiersma, Alessandra Candian, Joost M. Bakker, Annemieke Petrignani

Monthly Notices of the ROYAL ASTRONOMICAL SOCIETY

MNRAS **516,** 5216–5226 (2022) https://doi.org/10.1093/mnras/stac2627
Advance Access publication 2022 September 16

# Gas-phase spectroscopy of photostable PAH ions from the mid- to far-infrared

Sandra D. Wiersma [1,2,3★] Alessandra Candian [1] Joost M. Bakker [2] and Annemieke Petrignani [1★]

[1] *Van 't Hoff Institute for Molecular Sciences, University of Amsterdam, PO Box 94157, NL-1090 GD Amsterdam, the Netherlands*
[2] *Radboud University, Institute for Molecules and Materials, FELIX Laboratory, Toernooiveld 7, NL-6525 ED Nijmegen, the Netherlands*
[3] *Institut de Recherche en Astrophysique et Planétologie (IRAP), CNRS, Université de Toulouse (UPS), F-31028 Toulouse, France*

Accepted 2022 September 13. Received 2022 September 13; in original form 2021 November 17

## ABSTRACT

We present gas-phase InfraRed Multiple Photon Dissociation (IRMPD) spectroscopy of cationic phenanthrene, pyrene, and perylene over the 100–1700 $cm^{-1}$ (6–95 μm) spectral range. This range covers both local vibrational modes involving C–C and C–H bonds in the mid-IR, and large-amplitude skeletal modes in the far-IR. The experiments were done using the 7T Fourier-Transform Ion Cyclotron Resonance (FTICR) mass spectrometer integrated in the Free-Electron Laser for Intra-Cavity Experiments (FELICE), and findings were complemented with Density Functional Theory (DFT) calculated harmonic and anharmonic spectra, matching the experimental spectra well. The experimental configuration that enables this sensitive spectroscopy of the strongly bound, photoresistant Polycyclic Aromatic Hydrocarbons (PAHs) over a wide range can provide such high photon densities that even combination modes with calculated intensities as low as 0.01 km $mol^{-1}$ near 400 $cm^{-1}$ (25 μm) can be detected. Experimental frequencies from this work and all currently available IRMPD spectra for PAH cations were compared to theoretical frequencies from the NASA Ames PAH IR Spectroscopic Database to verify predicted trends for far-IR vibrational modes depending on PAH shape and size, and only a relatively small redshift (6–11 $cm^{-1}$) was found between experiment and theory. The absence of spectral congestion and the drastic reduction in bandwidth with respect to the mid-IR make the far-IR fingerprints viable candidates for theoretical benchmarking, which can aid in the search for individual large PAHs in the interstellar medium.

**Key words:** astrochemistry – methods: laboratory – techniques: spectroscopic – planets and satellites: atmospheres – ISM: molecules – infrared: ISM.

## 1 INTRODUCTION

Polycyclic aromatic hydrocarbons (PAHs) are one of the most stable families of organic molecules known. They are found in outer space, where they are formed through combustion-like chemistry in the outflows of carbon-rich stars (Allamandola, Tielens & Barker 1989; Latter 1991). The presence of PAHs has been established in many astronomical environments, and it has been estimated that PAHs comprise between 10 and 18 per cent of the elemental carbon budget (Joblin, Leger & Martin 1992; Tielens 2013). Since the interstellar PAH hypothesis was presented in 1984 (Leger & Puget 1984; Sellgren 1984), many astronomical observations, theoretical studies, and laboratory experiments have been conducted that have led to the conclusion that the dominant Aromatic Infrared Bands (AIBs) observed in the mid-infrared (MIR) at 3.3, 6.2, 7.7, and 11.3 μm can be attributed to emissions of UV-excited PAHs in the ISM (Allamandola et al. 1989; Hudgins & Allamandola 1995; van Diedenhoven et al. 2004; van Dishoeck 2004; Tielens 2008; Peeters 2011; Montillaud, Joblin & Toublanc 2013; Candian, Sarre & Tielens 2014; Andrews, Candian & Tielens 2016; Croiset et al. 2016; Bauschlicher et al. 2018). These and many other studies have helped put limits on the expected size of interstellar PAHs and elucidated details of their life cycles; it is now well-established that a large fraction of the PAH population in the ISM is present in cationic form (see Tielens 2008 and references therein).

Recently, the radio wave fingerprints of both pure and nitrogen-containing PAHs with two rings have been detected in the dark cloud TMC-1 (Burkhardt et al. 2021; Cernicharo et al. 2021; McGuire et al. 2021). Fingerprints of closely related species have also been detected, leading to the discovery of benzene and benzonitrile (Cernicharo et al. 2001; Kraemer et al. 2006; McGuire et al. 2018), as well as the fullerenes $C_{60}$, $C_{60}^+$, and $C_{70}$ (Cami et al. 2010; Sellgren et al. 2010; Berné, Mulas & Joblin 2013; Campbell et al. 2015; Cordiner et al. 2019). The presence of fullerenes has been confirmed by both their visible (Campbell et al. 2015; Cordiner et al. 2019) and MIR (Cami et al. 2010; Sellgren et al. 2010; Berné et al. 2013) fingerprints. Benzene, $C_{60}$, and $C_{70}$ possess characteristic IR emission lines that allowed interstellar MIR features to be assigned to them. However, an infrared match with the spectrum of a single PAH is still elusive, as PAHs in the MIR exhibit highly similar spectra, dominated by local C–C and C–H modes. This is especially true for a larger ones (>50

★ E-mail: sandra.wiersma@irap.omp.eu (SDW); a.petrignani@uva.nl (AP)

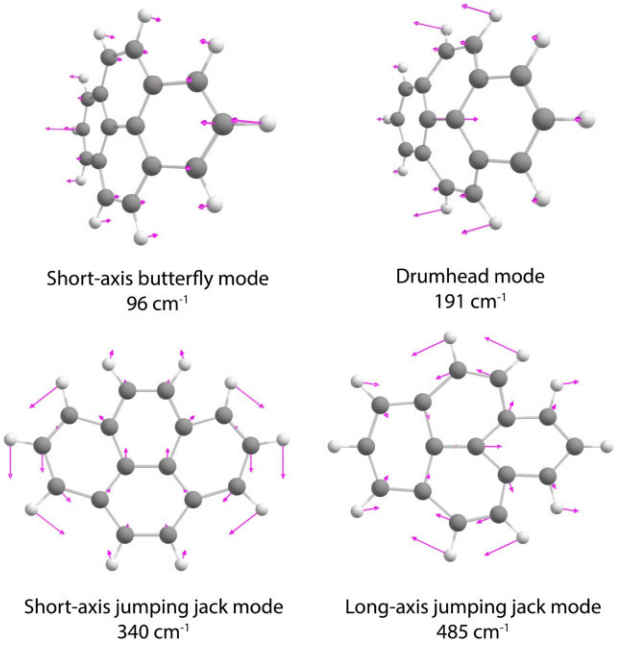


**Figure 1.** Skeletal vibrations of cationic pyrene, visualized with displacement vectors. The scaled frequencies are taken from the harmonic DFT calculations which are treated in Section 2.2 and listed from the drumhead mode on in Table 3.

C atoms), which are suspected to be the most abundant (Andrews et al. 2016).

The scenario is different for the far-infrared (FIR) fingerprints of PAHs. Here, global, skeletal deformation vibrations, with names such as drumhead, butterfly, or jumping jack modes (see Fig. 1) are much more molecule specific (Mulas et al. 2006a, b; Ricca et al. 2010, 2012). Although possible FIR PAH emission bands are often obscured by dust emissions in interstellar objects (Draine 2003), emission features in the MIR-to-FIR transition zone, at 15.8, 16.4, 17.4, 17.8, and 18.9 μm, have been attributed to PAHs (Boersma et al. 2010; Ricca et al. 2010). Further in the FIR, bands have been suggested to be even more characteristic for individual PAHs or PAH families (Mulas et al. 2006a, b; Boersma et al. 2011b, a; Joblin et al. 2011; Ricca et al. 2012). These studies are, however, entirely based on theoretical spectra from the NASA Ames PAH Database (Bauschlicher et al. 2018), for which the FIR benchmarking is primarily based on the spectrum of a single PAH, neutral naphthalene (Pirali et al. 2009).

Laboratory studies have revealed many characteristic IR spectral properties of PAHs, but have mostly been limited to wavelengths below 20 μm (above 500 $cm^{-1}$), which do not involve the truly global modes. Matrix isolation spectroscopy studies have mostly focused on neutral PAH species, partially due to difficulties in discriminating signal originating from ions or neutral (Leger, D'Hendecourt & Defourneau 1989; Blanco, Fonti & Orofino 1990; Moutou, Leger & D'Hendecourt 1995; Mattioda et al. 2009; Cataldo et al. 2013; Zhang & Sander 2017). Other difficulties including impurities and backgrounds exist for gas-phase FT-IR or emission spectroscopy (Kurtz 1992; Zhang et al. 1996; Cané et al. 1997; Pirali et al. 2006, 2009, 2013; Goubet & Pirali 2014). For neutral PAHs, ion-dip spectroscopy allows for detailed high-resolution investigations of, e.g. anharmonic behaviour; however, its application to ionic species is not trivial (Maltseva et al. 2015; Lemmens et al. 2019). To record laboratory spectra for gas-phase ions over large spectral ranges (covering mid- to far-IR), IR multiple-photon dissociation (IRMPD) spectroscopy is presently one of the most powerful methods (Oomens et al. 2000, 2006).

In this work, we used the high IR photon densities available in the Fourier Transform Ion Cyclotron Resonance (FT-ICR) mass spectrometer beamline of the FELICE intra-cavity free-electron laser to perform IRMPD spectroscopy of PAH cations in the FIR up to wavelengths of 100 μm. We present IRMPD spectra for phenanthrene ($C_{14}H_{10}^{+}$), pyrene ($C_{16}H_{10}^{+}$), and perylene ($C_{20}H_{12}^{+}$), in the range of 100–1700 $cm^{-1}$ with particular attention to the 100–600 $cm^{-1}$ FIR spectral range. We assign a large range of low-frequency bands using Density Functional Theory (DFT) calculations in both the harmonic and the anharmonic approximation. The narrow FIR modes in our experimental spectra are then considered as possible benchmarking data to improve the NASA Ames PAH Database in this spectral range (Bauschlicher et al. 2018). Finally, we discuss the implications of our findings for possible astronomical detection of molecule-specific signatures in the ISM.

## 2 METHODS

### 2.1 Experimental

IRMPD spectroscopy is a *multiple*-photon technique wherein absorption occurs repeatedly via the same transition. The absorbed energy is dissipated over a bath of dark vibrational states and once the fragmentation limit is overcome the species of interest can dissociate, signalling an IR active vibrational mode (Oomens et al. 2006). The multiple-photon character of IRMPD spectroscopy leads in general to slight spectral broadening and redshifts from the fundamental vibrational transition, as it is favourable to achieve fragmentation when higher transitions of the anharmonic vibrational ladder are also excited. Interestingly, the latter make the detected bands a closer representation for the emissions from hot, interstellar PAHs. IRMPD intensities tend to scale linearly with laser power and the single-photon absorption cross-section once a certain threshold is overcome (Oomens et al. 2006; Bakker et al. 2007; Berden et al. 2019) but because this threshold is band- and species-dependent, IRMPD spectra can differ from the linear absorption spectra.

The IRMPD spectra were recorded using the FT-ICR mass spectrometer beam line of the Free Electron Laser for Intra-Cavity Experiments (FELICE), at the FELIX Laboratory in Nijmegen. The FELICE FT-ICR apparatus, schematically shown in Fig. 2(a), has been described in detail before (Petrignani et al. 2016; Wensink et al. 2020). Here, additional experimental details are presented on features of the FELICE FT-ICR that were used for the first time in this work.

Phenanthrene, pyrene, and perylene (Sigma Aldrich/Merck) were brought into the gas phase using an effusive sublimation source, at temperatures of 50, 70, and 130°C, respectively. The gas-phase PAHs were then exposed to 20-eV electrons in an electron impact ionizer (Ardara Technologies), creating singly-charged radical cations. These cations were led through a series of ion optics, including a linear quadrupole mass spectrometer (QMS) operated in radio-frequency guiding mode and collected a sectioned, quadrupole ion trap with rectilinear rods (RIT), and collisionally cooled with argon gas (∼$10^{-2}$ mbar) (Ouyang et al. 2004). After accumulating and cooling over 50 ms in the RIT, an ion pulse was extracted towards an intra-cavity quadrupole deflector (IQD), which diverted the ion trajectory by 90° into the FELICE cavity. A home-built intra-cavity radiofrequency quadrupole ion guide (IQG) transported the ions towards one of the four FT-ICR storage cells. For each cell, the

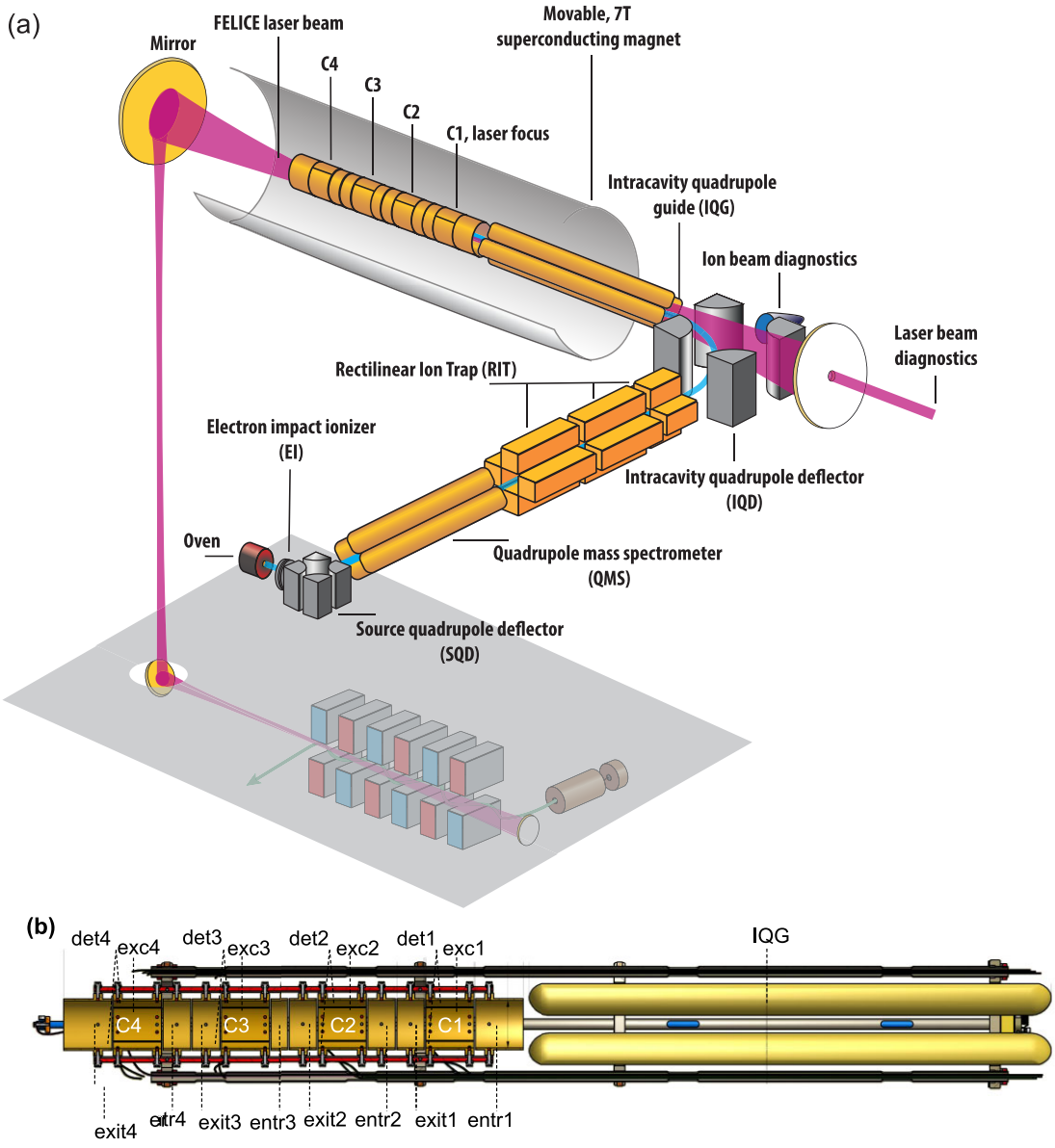


**Figure 2.** (a) Schematic of the FELICE FT-ICR instrument. The path of the molecules through the apparatus from the sublimation source down to the ICR cells is depicted in blue. The fuchsia beam illustrates the FELICE waist through the cavity. Proportions in this figure are not to scale. (b) Cross section of the four storage cells (C1–4) and the intra-cavity quadrupole ion guide (IQG). The ions move from right to left and are stored in one of the storage cells (C#). The top and side plates are used as excitation (exc#) and detection (det#) plates, respectively. When using one cell, the electrodes of all other cells are grounded. The focus of the FELICE laser beam coincides with the centre of C1, and is characterised by a 82 mm Rayleigh length.

mass resolution exceeds $m/\Delta m = 10^5$ for mass-to-charge ratios of up to at least 1000 m/z.

The FT-ICR storage cells are labelled C1–C4, and are depicted in Fig. 2(b). These open-ended, cylindrical cells (5 cm diameter) are located within a movable 7-Tesla superconducting magnet (Cryomagnetics Inc.). This magnet can be positioned in such a way that the volume of homogeneous magnetic field (<19 ppm) overlaps with the centre of either of the four cells. The multicell configuration was introduced to enable IR spectroscopy with varying IR fluences inside the laser cavity. C1 is positioned in the laser focus, and ions stored here experience the largest laser fluence. With a spacing between the cells of 10 cm, and the laser Rayleigh range of 82 mm, ions in each next cell are submitted to a fluence reduced by a factor of 2.3. For compounds with a relatively strong absorption efficiency, spectroscopy is preferably done in C4, as the overlap between the ion cloud and the laser beam is larger, and the reduced fluence will lead to less spectral broadening. C1 is used for the most photostable species or weakest absorptions. For pyrene and perylene, spectra were recorded in C4 in the 600–1700 $cm^{-1}$ spectral range, and spectra at lower frequencies in C1. For phenanthrene, the 235–650 $cm^{-1}$ spectral range was recorded using C4, and the 105–300 $cm^{-1}$ range in C1.

After transfer to the selected cell, the cations of interest were mass-isolated via a stored waveform inverse Fourier Transform (SWIFT) pulse (Marshall, Hendrickson & Jackson 1998). The ions were then exposed to one or several (max. 20) FELICE macropulses, depending

on the spectral range and studied molecule. At 1000 $cm^{-1}$ (10 μm), fragmentation for a PAH cation requires more than 6 eV or 50 photons to break a C–H bond, translating to more than 600 photons at (100 $cm^{-1}$) 100 μm (Ricca et al. 2012). For each spectrum, the IR frequency was scanned in steps of 1, 2.5, or 5 $cm^{-1}$, depending on the spectral range. At each frequency step, 5–20 time transients were averaged and Fourier transformed. The whole experimental sequence is controlled by home-built software developed by Mize et al. (2004).

The IRMPD spectrum was obtained by monitoring the fragmentation yield $Y(\nu)$ at wavenumber $\nu$, defined as

$$Y(\nu) = \ln\left(\frac{-N_{\rm par}(\nu)}{N_{\rm par}(\nu) + N_{\rm frag}(\nu)}\right) \quad (1)$$

with $N_{\rm frag}$ and $N_{\rm par}$ as the total fragment and parent mass counts, respectively. $Y$ is then divided by $P(\nu)$, the macropulse energy, which is inferred from coupling a fraction of the light out through a 1 mm-diameter hole of the cavity end mirror, and directing it on to a power meter. The IR wavelength was calibrated using a grating spectrometer (Princeton Instruments SpectraPro). The 100–1700 $cm^{-1}$ spectral range was recorded with three separate FEL settings. In the 600–1800 $cm^{-1}$ range, the FELICE macropulse energy peaked between 1500 and 1600 $cm^{-1}$ at 1.6 J. In the 200–600 $cm^{-1}$ range, it was slightly lower with its maximum at 1.3 J around 475 $cm^{-1}$. For the 100–300 $cm^{-1}$ range, the maximum was reached around 275 $cm^{-1}$ at 0.4 J. In spite of attempts to moderate the macropulse energy, saturation of the strongest bands in the 1000–1800 $cm^{-1}$ wavenumber range occurred. For these bands, all ions overlapped by the laser fragmented, leading to a maximum in the fragmentation yield. Saturated peak heights in the spectrum are still modulated by the power correction. After power correction of the three individual curves, they are joined by normalizing to the overlapping resonances, or in the case there is no overlapping resonance, by correcting for the drop in fluence from one cell to the next. The composite spectrum is then normalized to the resulting highest intensity, giving the final normalized IRMPD yield. For the presented experiments, 4–10 μs long macropulses were used, at a FELICE repetition rate of 5 or 10 Hz, which in turn consist of ps-long micropulses at 1 GHz. The spectral bandwidth (FWHM) was ∼0.6 per cent of the central wavelength (in μm).

### 2.2 Computational

DFT calculations were employed to predict the IR spectra and compare to experiment, using the Gaussian16 Suite (Frisch et al. 2016). For all three molecules, geometry optimizations, and harmonic vibrational calculations were performed using the B3LYP functional (Lee, Yang & Parr 1988; Becke 1993) and 6-311++G(2d,p) (Frisch, Pople & Binkley 1984) basis set. The harmonic calculations were scaled to match the experimental frequencies by a factor of 0.96. For pyrene and perylene, we present both the scaled harmonic calculations and unscaled anharmonic calculations at the B3LYP/N07D level of theory (Barone, Cimino & Stendardo 2008; Mackie et al. 2018). The individual modes are visualized and identified using the computational chemistry software suite GABEDIT (Allouche 2011). We adopted the FIR mode naming conventions introduced by Ricca et al. (2010).

## 3 RESULTS

The fragments observed in the IRMPD spectroscopy of the three respective PAHs are listed in Table 1. The smallest PAH ion, phenanthrene, exhibits both H and hydrocarbon loss. For pyrene, H-loss is dominant, and the hydrocarbon loss is very weak. For perylene, only H-loss is observed. This follows previously established experimental trends for cationic PAHs using IRMPD (Bouwman et al. 2019), collision-induced dissociation (West, Lesniak & Mayer 2019), and UV-photodissociation (Ekern et al. 1998). Theoretical studies on the reaction paths for [2C, 2H] loss processes showed that pericondensed PAHs lack the structural flexibility to form the four- and five-ringed intermediates necessary for [2C, 2H] loss, and that structural rigidity increases for larger, more aromatically stabilized PAHs (Holm et al. 2011; West et al. 2019). Furthermore, the ease with which −2H/-H2 is lost from highly-excited large PAHs is also reflected in other work (Zhen et al. 2014, 2017, 2018; Castellanos et al. 2018; Rodriguez Castillo, Simon & Joblin 2018).

The IR spectra of the respective PAH ions were constructed according to equation (1) using the fragments listed in Table 1 followed by power correction and normalization, providing the normalized IRMPD yield. Minor loss channels (italicised) were omitted due to their low S/N ratios.

### 3.1 Phenanthrene

The IR spectrum of cationic phenanthrene ($C_{14}H_{10}{}^{+}$, $m/z = 178$) is shown in the 105–650 $cm^{-1}$ spectral range in Fig. 3 (black, top). The spectrum is a composite of two scans, which overlap between 240 and 290 $cm^{-1}$. Four well-resolved resonances are found for which frequencies and intensities are listed in Table 2. The bandwidths observed are roughly 20 $cm^{-1}$ full-width at half-maximum (FWHM), except for the 199 $cm^{-1}$ band, which has a width of ∼5 $cm^{-1}$. We attribute this smaller bandwidth to a reduction of the power broadening at longer wavelengths, to the reduced FEL spectral bandwidth, and a possibly diminished anharmonicity of lower frequency modes (Joblin et al. 1995; Oomens et al. 2006; Lemmens et al. 2020; Chakraborty et al. 2021). The 390 $cm^{-1}$ band exhibits a high-frequency shoulder, and the 571 $cm^{-1}$ band is asymmetric, both likely caused by underlying low-intensity resonances. The shown spectrum partially overlaps the IR spectra reported by Piest et al. (2001). Piest et al. (2001) presents the IRMPD spectrum of the phenanthrene cation and an IR photodissociation spectrum of the cold phenanthrene-Ar cation down to approximately 400 $cm^{-1}$. For the untagged phenanthrene cation, a band was observed at 578 $cm^{-1}$, while the tagged spectrum reported bands at 482 and 581 $cm^{-1}$. The same publication also reported multiple Franck–Condon active vibrational states detected via mass-analysed threshold ionization (MATI) further into the FIR, of which only the band at 402 $cm^{-1}$ matches with this work; the other reported bands are IR-inactive. The results from Piest et al. are consistent with this work, with a maximum frequency deviation of 10 $cm^{-1}$.

Our DFT-calculated spectrum of phenanthrene is also shown in Fig. 3 (bottom panel, red) with the calculated frequencies scaled by a factor of 0.96 and listed in Table 2. To facilitate comparison with the experiment, the stick spectrum is convolved with a Gaussian line shape function with a 30 $cm^{-1}$ FWHM. One can observe that there is a good agreement between calculated and experimental band positions. The calculated relative intensities compare reasonably well, with the largest mismatch for the 479 $cm^{-1}$ experimental band, which is predicted far weaker than observed. The high-frequency shoulder of the 390 $cm^{-1}$ band is rationalised by a (weak) predicted band at 420 $cm^{-1}$, and the raised baseline between the 479 and 571 $cm^{-1}$ bands is attributed to a calculated band at 532 $cm^{-1}$. A detailed comparison between the experiment and the DFT calculation can be found in Table 2, along with descriptions of the vibrational modes.

**Table 1.** Cationic fragment masses detected in the IRMPD spectroscopy of phenanthrene ($C_{14}H_{10}^+$, $m/z$ = 178), pyrene ($C_{16}H_{10}^+$, $m/z$ = 202), and perylene ($C_{20}H_{12}^+$, $m/z$ = 252). The dominant channel/fragment is denoted in bold. Detected fragment channels that were too weak to be included in the IRMPD spectra are listed in italic.

| $C_{14}H_{10}^+$ $m/z = 178$ | | $C_{16}H_{10}^+$ $m/z = 202$ | | $C_{20}H_{12}^+$ $m/z = 252$ | |
|---|---|---|---|---|---|
| fragment $m/z$ | loss of | fragment $m/z$ | loss of | fragment $m/z$ | loss of |
| 177 | -H | 201 | -H | 251 | -H |
| **176** | **− 2 H** | **200** | **−2 H** | **250** | **− 2 H** |
| 152 | −[2C, 2 H] | 199 | −3 H | 249 | −3 H |
| 151 | −[2C, 3H] | 198 | −4 H | 248 | −4 H |
| 150 | −[2C, 4H] | *176* | *−[2 C, 2 H]* | *246* | *−6 H* |
| | | *174* | *−[2 C, 4 H]* | | |

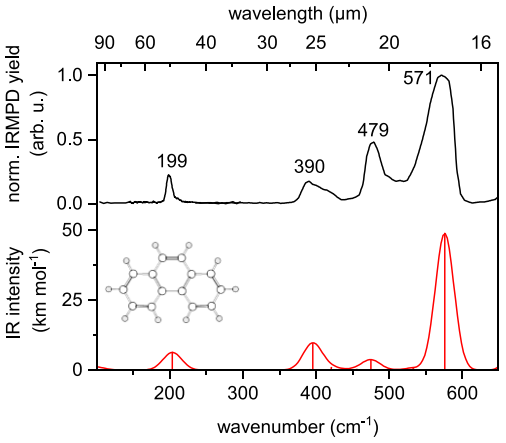


**Figure 3.** The experimental IRMPD spectrum (top) and theoretical IR spectrum (bottom) of cationic phenanthrene. The harmonic theoretical stick spectrum is scaled with a factor 0.96, and convolved with a 30 $cm^{-1}$ FWHM Gaussian line shape function.

**Table 2.** Phenanthrene cation observed band frequencies ($cm^{-1}$) and relative intensities, together with calculated frequencies ($cm^{-1}$) and IR intensities (km $mol^{-1}$), and descriptions of the theoretical modes. The listed harmonic frequencies are scaled by a factor 0.96. *oop: out-of-plane; ip: in-plane; E/C: elongation/compression*.

| Experiment | | Harmonic calc. | | Mode description |
|---|---|---|---|---|
| Freq. ($cm^{-1}$) | Norm. $Y$ | Freq. ($cm^{-1}$) | IR int. (km $mol^{-1}$) | |
| 199 | 0.22 | 204 | 6.3 | long-axis butterfly |
| 390 | 0.18 | 395 | 9.5 | quarto $HCCH_{oop}$ twist, duo $CH_{oop}$ wag |
| | | 420 | 0.9 | armchair ring rock |
| 479 | 0.48 | 475 | 3.7 | ip rock central ring, E/C outer phenyls |
| | | 532 | 0.7 | E/C middle ring |
| 571 | 1.00 | 576 | 48.9 | E/C outer phenyls |

These mode descriptions show that as we move further into the FIR, the skeletal motions become increasingly out-of-plane.

### 3.2 Pyrene

The IR spectrum of cationic pyrene ($C_{14}H_{10}^+$, $m/z$ = 202 amu) is shown in Fig. 4(a) (black curve, top panel). It spans the range of 110–1590 $cm^{-1}$ and consists of a composite of three individual curves, which overlap between 240–300 $cm^{-1}$ and 560–600 $cm^{-1}$. We observe twelve distinct bands, for which frequencies and intensities are listed in Table 3. The bands at 1320 and 1381 $cm^{-1}$ have almost merged, but two distinct shapes can still be discerned. The observed bandwidths vary between approximately 40 and 60 $cm^{-1}$ in the range between 450 and 1590 $cm^{-1}$, decrease to 30 $cm^{-1}$ for the features at 335 and 434 $cm^{-1}$, and drop sharply to 3 $cm^{-1}$ for the feature at 188 $cm^{-1}$. The spectrum between 1000–1600 $cm^{-1}$ is possibly affected by saturation due to the high power and strong absorptions; as a consequence, laser power normalization leads to an underestimation of the relative intensity. Although the high power may thus lead to saturation, it also enables the detection of very weak modes, especially in the FIR. A vertical close-up (black, dotted curve) in the FIR section clearly reveals modes at 335 and 434 $cm^{-1}$ with a high signal-to-noise (S/N) ratio, and predicted intensities of only 1.2 and 0.5 km $mol^{-1}$, respectively. These are around two orders of magnitude weaker than the strongest band in the MIR experimental spectrum.

The 600–1590 $cm^{-1}$ region of our spectrum agrees well with a previously reported spectrum of Oomens et al. (2000) in terms of peak positions and band shapes. We detect an additional band at 1100 $cm^{-1}$ and confirm the band at 990 $cm^{-1}$, which was detected at a very low S/N ratio in the previous work. Panchagnula et al. (2020) also published an IRMPD spectrum of pyrene in their Supplementary Material, in the 600–1700 $cm^{-1}$ range, which matches even better with our spectrum. They reproduced both our experimentally observed 990 and 1100 $cm^{-1}$ bands with a similarly high S/N, and the shape and peak positions line up nicely. In their main paper, they presented a high-resolution IR photodissociation spectrum of cold, neon-tagged pyrene in the same range. Many of the narrow bands in that spectrum fall under one, broadened feature in their IRMPD spectrum. Notably, the left shoulders on the 840, 990, and 1230 $cm^{-1}$ bands in our spectrum can be explained by blending of the higher-intensity transitions with lower-intensity features. Furthermore, Panchagnula et al. report a band at 768 $cm^{-1}$ where we do not observe any fragmentation. The agreement is good, but this work exhibits a consistent redshift in the region of 1200–1600 $cm^{-1}$ compared to the Ne-tagged spectrum, to a maximum of 23 $cm^{-1}$, which we attribute to the single-photon character of tagging spectroscopy.

Fig. 4(a) also displays the scaled harmonic (red curve, middle panel) and the anharmonic (blue curve, bottom panel) DFT spectra. The relative intensities for both theoretical spectra match the experiments reasonably well, although there are notable deviations in intensity for the observed 671, 840, and 1515 $cm^{-1}$ bands. Most band frequencies in the scaled harmonic spectrum match within 10 $cm^{-1}$,

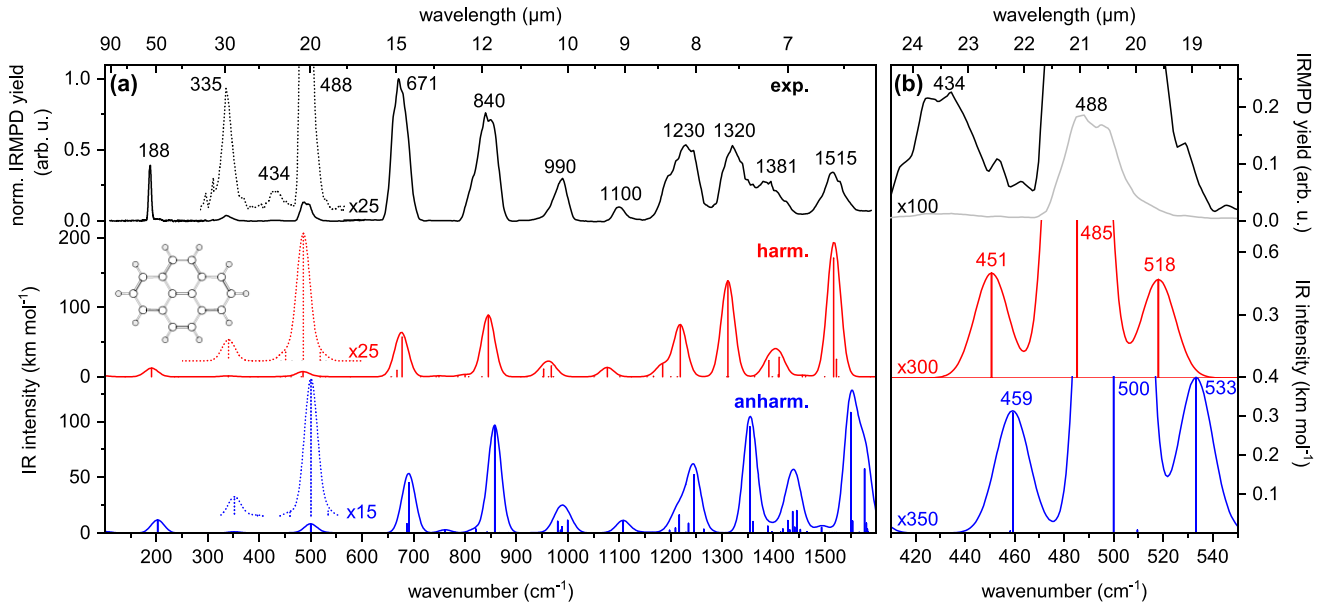


**Figure 4.** (a) The experimental IR spectrum of cationic pyrene (top, black), accompanied by DFT calculated spectra in harmonic (middle/red, frequencies scaled by a factor 0.96) and anharmonic (bottom/blue, unscaled) approximations; both calculated spectra are convolved with a 30 $cm^{-1}$ FWHM Gaussian line shape function. The dotted curves are vertical enlargements of the solid curves, slightly raised from the baseline for clarity. (b) Close-up of 400–550 $cm^{-1}$ spectral range of panel (a), with a convolution of 15 $cm^{-1}$ for both calculated spectra.

**Table 3.** Pyrene cation observed band frequencies ($cm^{-1}$) and relative intensities, together with calculated frequencies ($cm^{-1}$) and IR intensities (km $mol^{-1}$), and descriptions of the theoretical modes. The listed harmonic frequencies are scaled by a factor 0.96. *oop: out-of-plane; ip: in-plane; E/C: elongation/compression*.

| Experiment | | Harmonic calculations | | Anharmonic calculations | | |
|---|---|---|---|---|---|---|
| Freq. ($cm^{-1}$) | Norm. *Y* | Freq. ($cm^{-1}$) | IR int. (km $mol^{-1}$) | Freq. ($cm^{-1}$) | IR int. (km $mol^{-1}$) | Mode description |
| 188 | 0.390 | 191 | 12.4 | 203 | 11.7 | drumhead |
| 335 | 0.036 | 340 | 1.2 | 352 | 1.2 | short-axis jumping jack |
| 434 | 0.003 | 451 | 0.5 | 459 | 0.3 | long-axis $HCCH_{oop}$ twist |
| 488 | 0.130 | 485 | 7.3 | 500 | 8.3 | long-axis jumping jack |
| | – | 518 | 0.5 | 533 | 0.4 | short-axis E/C |
| 671 | 1.000 | 668 | 9.0 | 687 | 8.4 | long-axis E/C |
| | – | 678 | 57.2 | 691 | 45.3 | in-phase duo and trio $CH_{oop}$ wag |
| 840 | 0.759 | 845 | 88.7 | 858 | 95.7 | in-phase duo and trio $CH_{oop}$ wag |
| 990 | 0.298 | 953 | 11.1 | 981 | 10.6 | short-axis E/C |
| | – | 968 | 15.4 | 1000 | 11.5 | long-axis E/C |
| 1100 | 0.096 | 1077 | 13.4 | 1108 | 11.1 | antisymm. $CH_{ip}$ trio scissor |
| | – | 1184 | 17.3 | 1217 | 16.3 | – |
| 1230 | 0.533 | 1218 | 74.9 | 1246 | 52.4 | in-phase $CH_{ip}$ duo rock |
| 1320 | 0.528 | 1311 | 138.3 | 1354 | 95.2 | short-axis ipCC stretch |
| | – | – | – | 1360 | 10.2 | – |
| | – | – | – | 1389 | 6.3 | – |
| 1381 | 0.276 | 1391 | 23.2 | 1428 | 11.1 | $CH_{ip}$ scissor, short-axis $CC_{ip}$ stretch |
| | – | 1411 | 28.1 | 1437 | 19.3 | $CH_{ip}$ scissor, long-axis $CC_{ip}$ stretch |
| | – | – | – | 1445 | 20.3 | – |
| 1515 | 0.341 | 1517 | 171.2 | 1550 | 108.2 | $CH_{ip}$ scissor, short-axis $CC_{ip}$ stretch |
| | – | 1523 | 24.9 | 1577 | 57.6 | – |

except for the two experimental features at 990 and 1100 $cm^{-1}$. Here, the scaled harmonic positions at 953/968 $cm^{-1}$ and 1077 $cm^{-1}$ deviate 30–40 $cm^{-1}$ from experiment (see Table 3). These two bands are predicted better in the anharmonic calculation, which only deviate by 8 and 9 $cm^{-1}$, respectively. The peak positions of the 0-K anharmonic spectrum fall under the broad IRMPD features. This may reflect how the IRMPD spectra are measured at room temperature and are effectively redshifted from the 0-K band position.

Due to the sparse nature that the experimental and theoretical spectra exhibit in the FIR, unambiguous assignments are possible. Similar to the phenanthrene spectrum, the predicted FIR bands show activity in the entire skeletal frame, for which the exact descriptions are given in Table 3. Above 671 $cm^{-1}$, the modes become

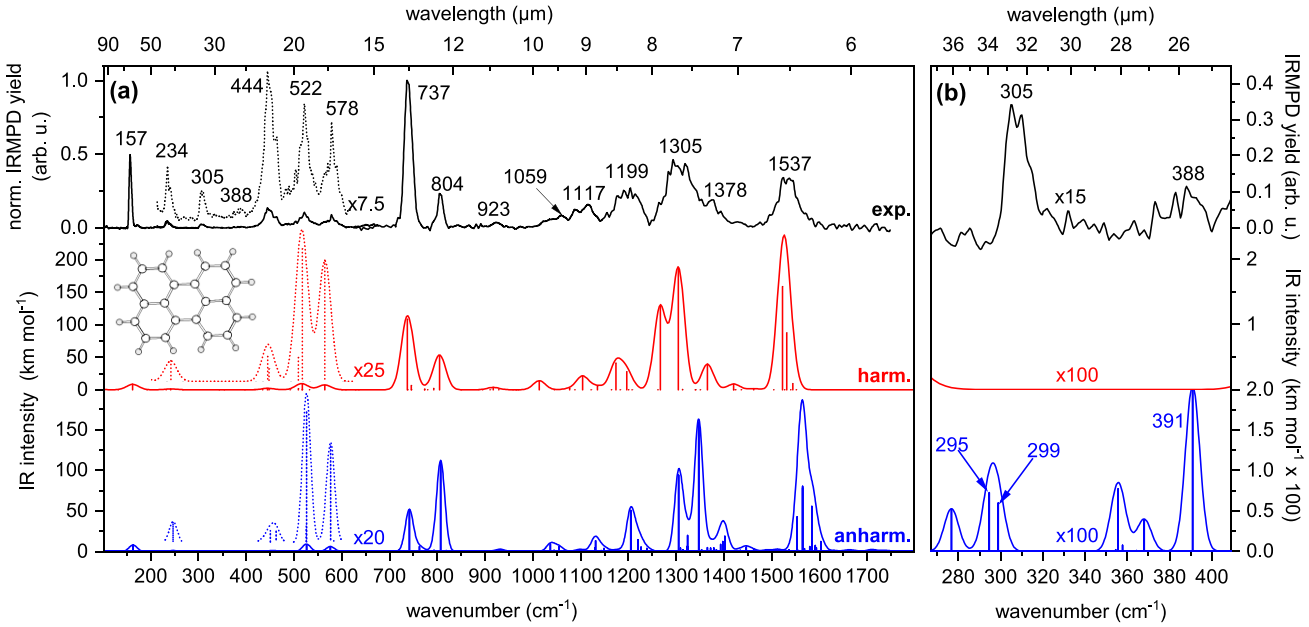


**Figure 5.** (a) The experimental IR spectrum of cationic perylene (top, black), accompanied by DFT calculated spectra in the harmonic (middle/red, frequencies scaled by a factor 0.96) and anharmonic (bottom/blue, unscaled) approximations; both calculated spectra are convolved with a 30 $cm^{-1}$ FWHM Gaussian line shape function. The dotted curves are vertical enlargements of the solid curves. (b) Close-up of 270–410 $cm^{-1}$ spectral range of panel (a) Note that the values on the y-axis of the two bottom panels have been multiplied by 100 for increased readability, and that the convolution has been decreased to 10 $cm^{-1}$.

increasingly local, and the experimental features are attributed to several close-lying local modes. The MIR assignments in Table 3 are therefore only given for the highest-intensity mode under the convolved peak.

Arguably, the weakest band is found at 434 $cm^{-1}$, a band that does not seem to be predicted in either of the DFT spectra. However, a close-up of this wavelength region in Fig. 4(b) shows that the strong, predicted band at 485/500 $cm^{-1}$ (harmonic/anharmonic) is accompanied by two much weaker satellites. The low-frequency satellite could very well account for the experimental 434 $cm^{-1}$ band, while the high-frequency satellite could account for the asymmetric lineshape of the experimental 488 $cm^{-1}$ band. Including anharmonicity does not provide a better match with the experiment. The calculated intensity of the harmonic 451 $cm^{-1}$ band has an intensity of only 0.5 km $mol^{-1}$. Our ability to detect this feature again demonstrates the high experimental sensitivity.

### 3.3 Perylene

For perylene ($C_{20}H_{12}^{+}$, $m/z = 252$ amu), the IR spectrum in the 105–1760 $cm^{-1}$ range is shown in Fig. 5(a) (black curve, top panel). The spectrum comprises three individual curves, with overlap between 215–300 $cm^{-1}$ and 620–675 $cm^{-1}$. In total, we observe sixteen bands (see Table 4) of which twelve can be clearly distinguished. The dotted curve shows a vertical enlargement for the weaker bands observed in the FIR, and clearly reveals high S/N bands at 234, 305, 388, 444, 522, and 578 $cm^{-1}$. The weakest 388 $cm^{-1}$ feature has a relative intensity three orders of magnitude lower than that for the highest-intensity observed band at 737 $cm^{-1}$. Bandwidths decrease for lower frequencies, down to 5 $cm^{-1}$ for the 188 $cm^{-1}$ band. The 188 $cm^{-1}$ band has a line width of 5 $cm^{-1}$. A previously reported spectrum of perylene for the MIR region (Bouwman et al. 2019), agrees well with our spectrum in that range. Band frequencies observed here are slightly redshifted (below 10 $cm^{-1}$) compared to Bouwman et al. (2019). Additionally, our work reveals two weak bands at 923 and 1059 $cm^{-1}$.

Scaled harmonic (red curve, middle panel) and anharmonic (blue/bottom) spectra are also shown in Fig. 5(a). The harmonic prediction agrees well with the experimental curve. Most peak positions are reproduced within 10 $cm^{-1}$, although in the 1000–1550 $cm^{-1}$ range, deviations of up to 18 $cm^{-1}$ occur, potentially due to saturation effects. As in pyrene, the peak positions of the 0-K anharmonic spectrum fall under the broad IRMPD features, showing what is likely a temperature-induced redshift. Following the same procedure as for phenanthrene and pyrene, the modes of most bands in the spectrum were assigned using the scaled harmonic spectrum, as listed in Table 4. The sparse FIR spectrum allowed for unambiguous assignment, whereas the more densely populated MIR shows several calculated transitions present under one merged band. In the MIR, the assignment corresponds with the highest-intensity mode(s) under such a peak. Similar to pyrene, the modes in the 600–1600 $cm^{-1}$ range have an increasing in-plane component for increasing frequency. In the FIR (100–600 $cm^{-1}$) region, we find skeletal out-of-plane and elongation/compression (E/C) modes.

The harmonic spectrum shows no intensity in the range between 300 and 400 $cm^{-1}$, where two features are observed experimentally at 305 and 388 $cm^{-1}$. Fig. 5(b) displays a deeper close-up of this range. The scaled harmonic curve only shows activity at the very edges. The anharmonic prediction shows minor activity, resulting from combination bands – not exceeding intensities above 0.02 km $mol^{-1}$. The 305 $cm^{-1}$ band is assigned to two combination bands calculated at 295 $cm^{-1}$ (the 133 $cm^{-1}$ H-C – C – H twist/scissor vibration and the 163 $cm^{-1}$ drumhead mode) and at 299 $cm^{-1}$ (two ring twisting modes at 26 and 274 $cm^{-1}$), whereas that at 388 $cm^{-1}$ is assigned to a combination band calculated at 291 $cm^{-1}$ (the 26 $cm^{-1}$ ring twisting mode and a 364 $cm^{-1}$ diagonal E/C mode). The experimental 388 $cm^{-1}$ feature is assigned to a combination band

**Table 4.** Perylene cation observed band frequencies ($cm^{-1}$) and relative intensities, together with calculated frequencies ($cm^{-1}$) and IR intensities (km $mol^{-1}$), and descriptions of the theoretical modes. The listed harmonic frequencies are scaled by a factor 0.96. *oop: out-of-plane; ip: in-plane; E/C: elongation/compression*.

| Experiment | | Harmonic calculations | | Anharmonic calculations | | |
|---|---|---|---|---|---|---|
| Freq. ($cm^{-1}$) | Norm. *Y* | Freq. ($cm^{-1}$) | IR int. (km $mol^{-1}$) | Freq. ($cm^{-1}$) | IR int. (km $mol^{-1}$) | Mode description |
| 157 | 0.495 | 162 | 8.4 | 163 | 8.0 | drumhead |
| 234 | 0.044 | 242 | 1.3 | 247 | 1.3 | short-axis jumping jack |
| | – | – | – | 295 | 0.007 | combination |
| 305 | 0.024 | – | – | 299 | 0.006 | combination |
| 388 | 0.001 | – | – | 391 | 0.024 | combination |
| 444 | 0.134 | 444 | 1.5 | 450 | 0.8 | long-axis jumping jack |
| | – | 447 | 0.8 | 462 | 0.8 | – |
| | – | 509 | 1.5 | 525 | 1.1 | – |
| 522 | 0.104 | 517 | 8.2 | 526 | 8.2 | zigzag $CH_{oop}$ wag |
| 578 | 0.087 | 564 | 7.5 | 576 | 6.1 | long-axis E/C |
| 737 | 1.000 | 737 | 108.8 | 741 | 51.5 | trio $CH_{oop}$ wag |
| | – | 746 | 6.5 | 762 | 6.1 | – |
| | – | 773 | 1.2 | 778 | 0.6 | – |
| | – | 793 | 2.1 | 793 | 1.5 | – |
| 804 | 0.232 | 805 | 52.1 | 807 | 110.2 | armchair $CH_{oop}$ wag |
| 923 | 0.035 | 917 | 3.6 | 931 | 2.5 | antiphase zigzag $CH_{oop}$, bay $CH_{oop}$ |
| | – | 1013 | 13.8 | 1037 | 9.1 | short-axis E/C |
| 1059 | 0.085 | 1077 | 1.8 | 1055 | 5.9 | trio $CH_{ip}$ scissor |
| 1117 | 0.157 | 1104 | 20.9 | 1131 | 13.2 | zigzag $CH_{ip}$ rock |
| | – | 1135 | 5.6 | 1149 | 3.9 | – |
| | – | 1174 | 41.0 | 1205 | 50.7 | antiphase armchair $CH_{ip}$ scissor |
| 1199 | 0.270 | 1197 | 27.5 | 1220 | 14.5 | in-phase zigzag $CH_{ip}$ rock |
| | – | 1267 | 128.3 | 1305 | 93.9 | antiphase bay $HCCCCH_{ip}$ scissor |
| | – | – | – | 1324 | 19.8 | – |
| 1305 | 0.462 | 1305 | 187.4 | 1347 | 158.4 | $CC_{ip}$ stretch |
| 1378 | 0.189 | 1365 | 39.4 | 1393 | 8.7 | armchair $CH_{ip}$ rock |
| | – | 1421 | 8.7 | 1398 | 12.5 | – |
| | – | – | – | 1402 | 18.8 | – |
| | | 1523 | 158.8 | 1553 | 42.6 | zigzag $CC_{ip}$ stretch, zigzag $HCCCH_{ip}$ scissor |
| 1537 | 0.341 | 1531 | 87.4 | 1564.6 | 78.4 | antiphase armchair $CC_{ip}$ stretch |
| | – | 1544 | 9.5 | 1565.0 | 80.4 | – |
| | – | – | – | 1584 | 55.7 | – |
| | – | – | – | 1603 | 12.5 | – |

predicted at 391 $cm^{-1}$ with an intensity of 0.024 km $mol^{-1}$, which is a combination of an IR-inactive ring twisting mode at 26 $cm^{-1}$ and an IR-inactive diagonal E/C mode, at 364 $cm^{-1}$. Calculation predicts an opposite intensity ratio between the two features observed in experiment. It may very well be that the closeness of the 295 and 299 $cm^{-1}$ bands leads to cooperative absorption, resulting in one stronger resonance.

## 4 DISCUSSION

The MIR-to-FIR spectra presented in this work are the first spectra of gas-phase, cationic PAHs to go down to 100 $cm^{-1}$, with bands below 200 $cm^{-1}$ having bandwidths of $\leq$5 $cm^{-1}$. These spectra represent an important venture into the FIR, adding to very limited experimental data (Bakker et al. 2010). There is no theoretical limit to how large a PAH can become before it becomes impossible to measure its FIR IRMPD spectrum. Although reduced IR cross sections, laser fluence, and photon energy will inevitably form a practical barrier, this has not been reached yet, and spectra of larger, more astronomically representative PAHs will likely be within the measurable range. As anharmonic effects at the basis of redshifts and line broadening are not well-understood in the FIR, especially narrow experimental bands might be more suitable than calculated bands in comparison to interstellar features. Beyond this measurable range, noble-gas tagging IRMPD spectroscopy becomes a potent method.

Astronomical FIR spectroscopy has been proposed in various studies as a method for molecule-specific PAH identification in the ISM (Mulas et al. 2006a, b; Boersma et al. 2011b, a; Ricca et al. 2010, 2012). Such studies ended up largely fruitless due to the lack of astronomical sensitivity at the time. With the *Origins Space Telescope* (*OST*) mission on the horizon, we are hopeful that efforts to find FIR signatures will be reinvigorated. With its high-resolution OSS and HERO FIR instruments, the *OST* mission will provide a resolution and sensitivity that are orders of magnitude better than Herschel's PACS and AKARI's FIS instruments were able to offer (Battersby et al. 2018). This mission thus offers a realistic (and exciting) prospect to discern PAH FIR modes from the dust background.

The improvements on the observation that *OST* will bring require an increased accuracy for the theoretical predictions. All FIR calculations have so far been benchmarked one experimental value of neutral naphthalene alone (166.4 $cm^{-1}$; Pirali et al. 2009) as experimental data in the FIR is lacking. Here, we discuss the comparison with this work (pyrene and perylene) and a previous study by one of the authors of this work (anthracene and coronene; Bakker et al. 2010), following the approach of Ricca et al. (2010, 2012) and Boersma et al. (2011b, a).

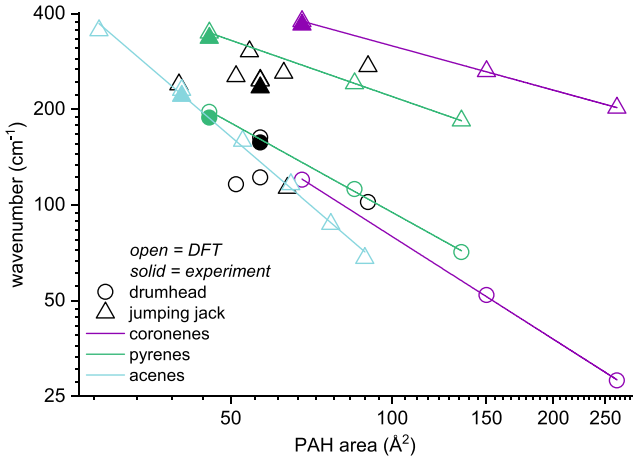


**Figure 6.** Double logarithmic plot of the harmonic DFT calculated (0,1) drumhead modes (circles) and short-axis jumping jack (triangles) for twenty cationic PAHs present in the NASA Ames PAH Database (PAHdb; Bauschlicher et al. 2018), together with experimentally observed band positions of four of these molecules as reported previously and in this work (open symbols) (anthracene and coronene from Bakker et al. (2010), and pyrene and perylene from this study). Linear fits of the predicted bands as function of PAH surface area for the different molecular families are given by the solid lines. A full list of included species is given in the Appendix. Cationic perylene was not present in the PAHdb, and we therefore used our own harmonic calculation, scaled with a factor of 0.96 to match in both the MIR and the FIR.

Fig. 6 shows the calculated FIR frequency trends for cationic PAHs as a function of PAH shape (family) and size (surface area $A$) together with the experimental data. Three PAH families (coronenes, pyrenes, and acenes) are displayed as well as an assorted set of PAHs that are capable of jumping-jack and/or drumhead vibrations (see Appendix for the complete list with further details). Also shown are the fitted trend lines for each predicted vibrational mode and family separately. The calculated values are taken from the NASA Ames PAH Database (PAHdb; Bauschlicher et al. 2018). Bond lengths are based on those of benzene (both C–C$\cong$1.39 Å and C–H$\cong$1.09 Å), after which we calculated the surface areas including H atoms in Å$^2$, for each PAH individually, using the geometries defined in Ricca et al. (2012). For clarity, only the drumhead modes with a single node (the (0,1) modes, circles), and short-axis jumping jack modes (triangles) are plotted.

There is an overall good agreement between experiment (open symbols) and PAHdb prediction (solid symbols). However, there is a systematic redshift of 6–11 cm$^{-1}$ of the experimental value with respect to the theoretical prediction. Two potential causes are the finite temperatures at which the experiments are conducted and the intrinsic red-shifting of IRMPD bands compared to the calculated fundamental $\nu = 1 \leftarrow \nu = 0$ transitions. This work could possibly contribute to new benchmarking efforts to improve predictions of FIR modes for hot, interstellar molecules.

As reported in Boersma et al. (2010), the drumhead modes (circles) are sensitive to PAH size, whereas the jumping-jack modes (triangles) are both strongly shape and size dependent. Indeed, the jumping-jack trend lines for each family are well separated, differing in offset and slope. Surprisingly, despite the strong shape dependence, the bent, single-row PAHs from the displayed assorted set follow the same jumping-jack trend as the linear acenes. This trend line seems to not necessarily be limited to the acene family. Interestingly, there is also a weak shape dependence of the drumhead modes visible, with the trend lines of the coronene and pyrene family similar, but separated. Benchmarking theory with accurate experimental data, especially for larger PAHs, can provide the means to fully disentangle shape from size dependence and identify individual PAHs. Given the current demonstration of IRMPD spectroscopy extended toward 100 μm, we foresee that such data will become available in the coming years (Boersma et al. 2011b).

Again, two mixed-shape PAHs, perylene and ovalene, follow the trend observed, potentially because both they and pyrenes in general have $D_{2h}$ symmetry. Because the drumhead trends for the coronenes and pyrenes show a weak, but significant difference, drumhead modes are slightly, but significantly shape dependent, contrary to what was previously postulated. Triphenylene and benzo[e]pyrene, two other mixed-shape molecules with a drumhead mode, do not coincide with the derived trend lines.

## 5 SUMMARY AND CONCLUSION

We present gas-phase spectra of cationic PAHs in the MIR to FIR region, up (down) to 100 μm (100 cm$^{-1}$). These spectra match our scaled, harmonic spectra very well. We also present anharmonic DFT calculations for cationic PAHs in the FIR, which we used to assign pure combination bands with a predicted intensity down to 0.006 km mol$^{-1}$. The lowest-frequency bands also match calculations from the PAHdb (Bauschlicher et al. 2018) fairly well, although a small, systematic redshift is found. The bandwidths below 200 cm$^{-1}$ are $\lesssim$5 cm$^{-1}$, making the IRMPD data in this wavelength range suitable for benchmarking efforts. In future studies, narrow FIR bands of astronomically sized PAHs – measured with IRMPD – would make good candidates for identification in astronomical surveys.

In this context, we revisited the hypothesis that FIR bands can be used to search for the IR emissions of single PAH species (Mulas et al. 2006a, b; Boersma et al. 2011b, a; Ricca et al. 2012). We report a larger dependence on molecular shape than was previously found, but emphasize the importance of reliable benchmarking before the deduced trends are used to search for astronomical features. Future experimental efforts should be focused on the measurement of FIR spectra of large, symmetric PAHs, both neutral and cationic. Using up to 20 FELICE macropulses, we were able to measure these FIR spectra. Although an upper limit for the size of PAH that we could measure is hard to determine without insight in the density of states, recent MIR studies using an extra-cavity FELIX setup on $C_{48}H_{18}+$ and $C_{48}H_{20}+$ give us confidence that at least this lower limit for astronomical PAHs is attainable Zhen et al. (2017, 2018). The future *OST* will be able to provide the sensitive observational data that is necessary to find these elusive FIR bands (Joblin et al. 2011; Battersby et al. 2018).

## ACKNOWLEDGEMENTS

We thank Dr. Christine Joblin for the insightful discussions and Prof. W.J. Buma for his thorough reading of an earlier version of the manuscript. We thank COST Action CA18212 – Molecular Dynamics in the GAS phase (MD-GAS), supported by COST (European Cooperation in Science and Technology). We gratefully acknowledge the *Nederlandse Organisatie voor Wetenschappelijk Onderzoek* (NWO) for the support of the FELIX Laboratory. This work is supported by the VIDI grant (723.014.007) of AP from NWO. Furthermore, AC gratefully acknowledges NWO for a VENI grant (639.041.543). Calculations were carried out on the Dutch national

e-infrastructure (Cartesius and LISA) with the support of Surfsara, under projects NWO Rekentijd 16260 and 17603.

## DATA AVAILABILITY

The data underlying this article is available at www.doi.org/10.21942/uva.17023880. Theoretical data from Fig. 6 is available at https://www.astrochemistry.org/pahdb/theoretical/3.20/default/view, and several experimental data points are derived from Bakker et al. (2010).

## REFERENCES


Allamandola L. J., Tielens G. G. M., Barker J. R., 1989, ApJS, 71, 733
Allouche A., 2011, J. Comput. Chem., 32, 174
Andrews H., Candian A., Tielens A. G. G. M., 2016, A&A, 595, A23
Bakker J. M., Besson T., Lemaire J., Scuderi D., Maître P., 2007, J. Phys. Chem. A, 111, 13415
Bakker J. M. et al., 2010, J. Chem. Phys., 132, 044501
Barone V., Cimino P., Stendardo E., 2008, J. Chem. Theory Comput., 4, 751
Battersby C. et al., 2018, Nat. Astron., 2, 596
Bauschlicher C. W., Ricca A., Boersma C., Allamandola L. J., 2018, ApJS, 234, 32
Becke A. D., 1993, J. Chem. Phys., 98, 5648
Berden G., Derksen M., Houthuijs K. J., Martens J., Oomens J., 2019, Int. J. Mass Spectrom., 443, 1
Berné O., Mulas G., Joblin C., 2013, A&A, 550, L4
Blanco A., Fonti S., Orofino V., 1990, ApJ, 364, 152
Boersma C., Bauschlicher C. W., Allamandola L. J., Ricca A., Peeters E., Tielens A. G. G. M., 2010, A&A, 511, A32
Boersma C. et al., 2011a, EAS Publ. Ser., 46, 109
Boersma C., Bauschlicher C. W., Ricca A., Mattioda A. L., Peeters E., Tielens A. G. G. M., Allamandola L. J., 2011b, ApJ, 729, 64
Bouwman J., Castellanos P., Bulak M., Terwisscha van Scheltinga J., Cami J., Linnartz H., Tielens A. G. G. M., 2019, A&A, 621, 80
Burkhardt A. M. et al., 2021, ApJ, 913, L18
Cami J., Bernard-Salas J., Peeters E., Malek S. E., 2010, Science, 329, 1180
Campbell E. K., Holz M., Gerlich D., Maier J. P., 2015, Nature, 523, 322
Candian A., Sarre P. J., Tielens A. G. G. M., 2014, ApJ, 791, L10
Cané E., Miani A., Palmieri P., Tarroni R., Trombetti A., 1997, Spectrochim. Acta A Mol. Biomol. Spectrosc., 53, 1839
Castellanos P., Candian A., Zhen J., Linnartz H., Tielens A. G. G. M., 2018, A&A, 616, 166
Cataldo F., Angelini G., Aníbal García-Hernández D., Manchado A., 2013, Spectrochim. Acta A, 111, 68
Cernicharo J., Heras A. M., Tielens A. G. G. M., Pardo J. R., Herpin F., Guélin M., Waters L. B. F. M., 2001, ApJ, 546, L123
Cernicharo J., Agúndez M., Cabezas C., Tercero B., Marcelino N., Pardo J. R., de Vicente P., 2021, A&A, 649, L15
Chakraborty S., Mulas G., Rapacioli M., Joblin C., 2021, J. Mol. Spectrosc., 378, 111466
Cordiner M. A. et al., 2019, ApJ, 875, L28
Croiset B. A., Candian A., Berné O., Tielens A. G. G. M., 2016, A&A, 590, A26
Draine B., 2003, Annu. Rev. Astron. Astrophys., 41, 241
Ekern S. P., Marshall A. G., Szczepanski J., Vala M., 1998, J. Phys. Chem. A, 102, 3498
Frisch M. J., Pople J. A., Binkley J. S., 1984, J. Chem. Phys., 80, 3265
Frisch M. J. et al., 2016, Gaussian 16 Revision C.01. Gaussian Inc., Wallingford CT
Goubet M., Pirali O., 2014, J. Chem. Phys., 140, 044322
Holm A. I., Johansson H. A., Cederquist H., Zettergren H., 2011, J. Chem. Phys., 134, 44301
Hudgins D. M., Allamandola L. J., 1995, J. Phys. Chem., 99, 3033
Joblin C., Leger A., Martin P., 1992, ApJ, 393, L79
Joblin C., Boissel P., Leger A., D'Hendecourt L., Defourneau D., 1995, A&A, 299, 835
Joblin C., Mulas G., Malloci G., Bergin E., 2011, EAS Publ. Ser., 46, 123
Kraemer K. E., Sloan G. C., Bernard-Salas J., Price S. D., Egan M. P., Wood P. R., 2006, ApJ, 652, L25
Kurtz J., 1992, A&A, 255, L1
Latter W. B., 1991, ApJ, 377, 187
Lee C., Yang W., Parr R. G., 1988, Phys. Rev. B, 37, 785
Leger A., Puget J. L., 1984, A&A, 137, L5
Leger A., D'Hendecourt L., Defourneau D., 1989, A&A, 216, 148
Lemmens A. K., Gruet S., Steber A. L., Antony J., Grimme S., Schnell M., Rijs A. M., 2019, Phys. Chem. Chem. Phys., 21, 3414
Lemmens A. K. et al., 2020, J. Phys. Chem. Lett., 11, 8997
Mackie C. J. et al., 2018, Phys. Chem. Chem. Phys., 20, 1189
Maltseva E. et al., 2015, ApJ, 814, 23
Marshall A. G., Hendrickson C. L., Jackson G. S., 1998, Mass Spectrom. Rev., 17, 1
Mattioda A. L., Ricca A., Tucker J., Bauschlicher C. W., Allamandola L. J., 2009, Astron. J., 137, 4054
McGuire B. A., Burkhardt A. M., Kalenskii S., Shingledecker C. N., Remijan A. J., Herbst E., McCarthy M. C., 2018, Science, 359, 202
McGuire B. A. et al., 2021, Science, 371, 1265
Mize T. H. et al., 2004, Int. J. Mass Spectrom., 235, 243
Montillaud J., Joblin C., Toublanc D., 2013, A&A, 552, A15
Moutou C., Leger A., D'Hendecourt L., 1995, A&A, 310, 297
Mulas G., Malloci G., Joblin C., Toublanc D., 2006a, A&A, 456, 161
Mulas G., Malloci G., Joblin C., Toublanc D., 2006b, A&A, 460, 93
Oomens J., van Roij A. J. A., Meijer G., von Helden G., 2000, ApJ, 542, 404
Oomens J., Sartakov B. G., Meijer G., von Helden G., 2006, Int. J. Mass Spectrom., 254, 1
Ouyang Z., Wu G., Song Y., Li H., Plass W. R., Cooks R. G., 2004, Anal. Chem., 76, 4595
Panchagnula S. et al., 2020, Phys. Chem. Chem. Phys., 22, 21651
Peeters E., 2011, Proc. Int. Astron. Union, 7, 149
Petrignani A., Vala M., Eyler J. R., Tielens A. G. G. M., Berden G., van der Meer A. F. G., Redlich B., Oomens J., 2016, ApJ, 826, 33
Piest J. A., Oomens J., Bakker J., von Helden G., Meijer G., 2001, Spectrochim. Acta A Mol. Biomol. Spectrosc., 57, 717
Pirali O., Van-Oanh N.-T., Parneix P., Vervloet M., Bréchignac P., 2006, Phys. Chem. Chem. Phys., 8, 3707
Pirali O., Vervloet M., Mulas G., Malloci G., Joblin C., 2009, Phys. Chem. Chem. Phys., 11, 3443
Pirali O. et al., 2013, Phys. Chem. Chem. Phys., 15, 10141
Ricca A., Bauschlicher C. W., Mattioda A. L., Boersma C., Allamandola L., 2010, ApJ, 709, 42
Ricca A., Bauschlicher C. W., Boersma C., Tielens A. G. G. M., Allamandola L. J., 2012, ApJ, 754, 75
Rodriguez Castillo S., Simon A., Joblin C., 2018, Int. J. Mass Spectrom., 429, 189
Sellgren K., 1984, ApJ, 277, 623
Sellgren K., Werner M. W., Ingalls J. G., Smith J. D. T., Carleton T. M., Joblin C., 2010, ApJ, 722, L54
Tielens A. G. G. M., 2008, Annu. Rev. Astron. Astrophys., 46, 289
Tielens A. G. G. M., 2013, Rev. Mod. Phys., 85, 1021
van Diedenhoven B., Peeters E., van Kerckhoven C., Hony S., Hudgins D. M., Allamandola L. J., Tielens A. G. G. M., 2004, ApJ, 611, 928
van Dishoeck E. F., 2004, Annu. Rev. Astron. Astrophys., 42, 119
Wensink F. J., Münst M. G., Heller J., Ončák M., Bakker J. M., Van Der Linde C., On M., Bakker J. M., 2020, J. Chem. Phys., 153, 171101
West B. J., Lesniak L., Mayer P. M., 2019, J. Phys. Chem. A, 123, 3569
Zhang X., Sander S. P., 2017, Chem. Phys. Lett., 688, 47
Zhang K., Guo B., Colarusso P., Bernath P. F., 1996, Science, 274, 582
Zhen J., Paardekooper D., Candian A., Linnartz H., Tielens A. G. G. M., 2014, Chem. Phys. Lett., 592, 211
Zhen J., Castellanos P., Bouwman J., Linnartz H., Tielens A. G. G. M., 2017, ApJ, 836, 28
Zhen J., Candian A., Castellanos P., Bouwman J., Linnartz H., Tielens A. G. G. M., 2018, ApJ, 854, 27

## SUPPORTING INFORMATION

Supplementary data are available at *MNRAS* online.

**Table S1:** List of PAH cations plotted in fig. 6 in the main paper, with their size in number of rings $R$ and their area $A$ in Å$^2$.

Please note: Oxford University Press is not responsible for the content or functionality of any supporting materials supplied by the authors. Any queries (other than missing material) should be directed to the corresponding author for the article.

This paper has been typeset from a TEX/LATEX file prepared by the author.